

## Multi-mission Observations of GS 1354-64 during the 2025-26 Outburst: First Results

DIPAK DEBNATH,<sup>1,2</sup> HSIANG-KUANG CHANG,<sup>1,3</sup> SUBHAM SRIMANI,<sup>1</sup> AND ANUJ NANDI<sup>4</sup>

<sup>1</sup>*Institute of Astronomy, National Tsing Hua University, Hsinchu 300044, Taiwan*

<sup>2</sup>*Institute of Astronomy Space and Earth Science, P 177, CIT Road, Scheme 7m, Kolkata 700054, India*

<sup>3</sup>*Department of Physics, National Tsing Hua University, Hsinchu 300044, Taiwan*

<sup>4</sup>*Space Astronomy Group, ISITE Campus, U R Rao Satellite Centre, Bengaluru, 560037, India*

(Accepted on May 15, 2026)

Submitted to ApJ

### ABSTRACT

The Galactic transient black hole GS 1354-64 recently showed a new outburst, which has been continuously monitored by *MAXI*, *NuSTAR* and *Insight-HXMT* missions. The ongoing 2025 – 26 outburst shows a slow-rise with an unusual short period ( $\sim 3$  days) of X-ray flare of peak flux  $\sim 1.4$  Crab, followed by another relatively weak flare of intensity  $\sim 0.8$  Crab. The source is observed to evolve through ‘canonical’ spectral states in a Hardness-Intensity Diagram (HID) during rising phase of the outburst, however subsequent outburst profile did not follow the reverse trend of the HID. A rapid evolution of Quasi-periodic Oscillation (QPO) frequencies ( $\sim 0.07 - 4$  Hz) is observed during hard/intermediate spectral states without any signature of QPOs in the soft state. The evolution of the observed low frequency QPOs shows a monotonically increasing (rising phase) as well as decreasing (decay phase) signature, which are further studied with the propagating oscillatory shock model to understand the nature of the evolution of the shock wave, responsible for the origin of the observed QPOs. The broadband energy spectra from *NuSTAR* (3 – 70 keV) and *Insight-HXMT* (2 – 60 keV) are well described by thermal (*diskbb*) and reflection (*relxill*) model components, indicating a strong signature of a relativistic reflection feature. Using ‘canonical’ softer state observations, we found the source to be maximally rotating with  $a_k \sim 0.998$  and inclination angle to be as  $i \sim 63^\circ - 70^\circ$ , which are consistent with earlier reports.

*Keywords:* X-ray binary stars(1811) – X-ray transient sources(1852) – Black holes(162) – Black hole physics(159) – Accretion(14) – Shocks (2086)

### 1. INTRODUCTION

Compact objects, mainly low mass X-ray binaries, are very fascinating astronomical objects to study in X-rays as they show variations in their properties in a short duration. Transient black hole X-ray binaries (BH-XRBs) are one of the excellent astronomical laboratories to understand the nature of these highly interesting systems (Y. Tanaka & W.H.G. Lemin 1995). Rapid evolution of spectral and temporal properties are seen during both rising and declining phases of an outburst of these BH-XRBs (see for e.g., R. A. Remillard & J. E. McClintock 2006; T. Belloni et al. 2005; A. Nandi et al. 2012; D. Debnath et al. 2015; H. Sreehari et al. 2019). Strong evidence of the correlations between the spectral

(photon index, disk temperature, election temperature etc.) and temporal (QPO frequency, rms, hardness-ratio etc.) features are observable (see for a review, R. A. Remillard & J. E. McClintock 2006). The different branches of the Hardness-Intensity Diagram (HID) or the AccRetion Rate Intensity Diagram are found to be linked with different spectral states characterized by distinct temporal features, including Quasi-periodic Oscillations (QPOs), jets, etc. (R.P. Fender et al. 2004; T. Belloni et al. 2005; J. Homan & T. Belloni 2005; A. Jana et al. 2016; D. Radhika et al. 2016; S.D. Choudhury et al. 2025). Generally, four spectral states: low-hard (LHS), hard-intermediate (HIMS), soft-intermediate (SIMS) and high-soft (HSS) are observed during a classical or type-I outburst of a transient BH candidate, while softer states are found to be missing during a harder or type-II outburst (D. Debnath et al. 2017). These spectral states also show a hysteresis loop with LHS as a start

and end phase of the outburst (J. Homan & T. Belloni 2005; A. Nandi et al. 2012; D. Debnath et al. 2013; H. Sreehari & A. Nandi 2021).

Transient BH-XRBs generally remain in low luminosity ( $L_X \sim 10^{30-33} \text{ erg s}^{-1}$ ; B.E. Tetarenko et al. 2016) quiescence phases, and occasionally become active for a period of weeks to months. During these active or outbursting phases, the sources become extremely luminous ( $L_X \sim 10^{37-38} \text{ erg s}^{-1}$ ; Y. Tanaka & N. Shibazaki 1996). It is generally believed that an outburst is triggered due to a sudden rise of viscosity at the outer edge of the accretion disk (K. Ebisawa et al. 1996). Recently S.K. Chakrabarti et al. (2019) has introduced the concept of accumulation of mass from the companion donor star at a temporary reservoir, namely the pile-up radius ( $X_p$ ), located at a far distance between the BH and Lagrange point L1. In a quiescence or accumulation phase, viscosity as well as instability increases at  $X_p$  with the increase of the accumulated matter. The onset of an outburst occurs due to the rapid inflow of accumulated matter toward the BH when the viscosity exceeds a critical threshold, which depends on  $X_p$ . The triggering mechanism of type-I and type-II outbursts has quite successfully explained different types (time period, intensity, peak flux etc.) of outbursts in three recurring transient BH candidates: H 1743-322 (S.K. Chakrabarti et al. 2019), GX 339-4 (R. Bhowmick et al. 2021), 4U 1630-47 (K. Chatterjee et al. 2022).

The electromagnetic radiations that we observe in multi-wavelength bands, are emitted from the accretion disk formed around the compact object. The continuum part of the energy spectrum of a BH-XRB, mainly consists of two components: one multi-color thermal disk black body emission from the accretion disk (K. Mitsuda et al. 1984; K. Makishima et al. 1986) and another non-thermal power-law tail, which originated from the Corona or Compton cloud due to inverse-Comptonization of disk photons (R.A. Sunyaev & L.G. Titarchuk 1980, 1985). Several models have been proposed to explain the nature and origin of this ‘Compton cloud’, such as a magnetic corona (A.A. Galeev et al. 1979) and a hot gas corona above the disk (F. Haardt & L. Maraschi 1993; A. A. Zdziarski et al. 2003; C. Done et al. 2007). In the context of two component advective flow model (S.K. Chakrabarti & L. Titarchuk 1995), accretion disk contains two different types of flows. First one is high viscous, high angular momentum, geometrically thin and optically thick Keplerian disk matter, which forms a standard disk at the equatorial plane (N.I. Shakura & R.A. Sunyaev 1973) and acts as the source of observed thermal black body photons. The other flow component is a low-viscous, low-angular-momentum, optically thin, and geometrically thick sub-Keplerian halo (flanked above and below the Keplerian disk), which forms a ‘hot’ puffed-up region (i.e., the corona) due to a shock transition

(S. K. Chakrabarti 1996a,b). This corona acts as a Compton cloud where thermal disk black body photons from the Keplerian disk become energetic hard photons via multiple inverse-Compton scattering (R.A. Sunyaev & L.G. Titarchuk 1980, 1985). Conversely, hard photons might be generated through upscattering of soft photons via synchrotron processes (e.g., G. Wardziński & A.A. Zdziarski 2000; A. Veledina et al. 2011). Furthermore, a third component may be present in the BH spectrum, characterized by the reflection of hard photons from the disk due to Compton down-scattering and atomic absorption or re-emission (A.P. Lightman et al. 1988; A.C. Fabian et al. 1989; L.W. Brenneman 2006; C. Bambi et al. 2010; J. García & T.R. Kallman 2010). Occasionally a prominent feature of characteristic line emission from various elements (e.g., the 6.5 keV Fe  $K_\alpha$  line) is observed in BH spectra (K. Makishima 1986; A.C. Fabian et al. 1989). Moreover, the observed skewed Fe  $K_\alpha$  line and reflection signatures are considered to be strong relativistic effects induced by the spin of the black hole (J. García & T.R. Kallman 2010; C.S. Reynolds 2014).

Low frequency (0.01 – 30 Hz) QPOs (LFQPOs) are commonly observed in hard and intermediate spectral states of BH-XRBs (see, R. A. Remillard & J. E. McClintock 2006). Depending upon the nature (fundamental frequency, rms, Q-value, noise, lag, etc.), QPOs are classified into three main types: A, B, C (P. Casella et al. 2005). In the LHS and HIMS of both rising and declining phases LFQPOs (type-C) are found to evolve monotonically, while in the SIMS QPOs (type-A or -B) are observed to the sporadically on and off without any detection in HSS. Many model have been proposed to explain origin of these QPOs, for example, magneto-acoustic waves (L. Titarchuk et al. 1998), spiral density waves (P. Varnière & M. Tagger 2002), Lense-Thirring precession (L. Stella & M. Vietri 1999), shock oscillation model (D. Molteni et al. 1996; D. Ryu et al. 1997; S.K. Chakrabarti et al. 2015). In the past, attempts also have been made to understand the evolution of QPO frequencies observed in various BH-XRBs (F. Vignarca et al. 2003; L. Titarchuk & E. Seifina 2009; H. Stiele et al. 2013, and references therein). However, according to the shock oscillation model, oscillation of the shock is considered as the origin of different types of QPOs. Type-C QPOs occur due to the resonance oscillation of the shock (when cooling and in-fall time scales roughly matches), while type-B QPOs originate from either non-satisfaction of the Rankine-Hugoniot conditions (necessary for stable shock formation) or a weakly resonating corona. The possible origin of the broader type-A QPOs might be due to the weak oscillations of the shockless centrifugal barrier (see S.K. Chakrabarti et al. 2015). Furthermore, time varying form of the shock oscillation model, namely propagating oscillatory shock (POS) model is

found to be quite successful for understanding of monotonic evolution of the QPO frequencies during the rising and declining phases of the outbursts of many transient BH-XRBs (see for example, S.K. Chakrabarti et al. 2008; A. Nandi et al. 2012; D. Debnath et al. 2013, 2025). Due to the monotonic rise in the QPO frequency, inward shock motion is observed during the rising phase of the outburst, while the reverse scenario is observed during the declining phase, as the QPO frequency is found to decrease monotonically.

GS 1354–64 (= BW Cir) is one of the dynamically confirmed stellar-mass BH-XRBs. It was discovered by the *Ginga* satellite in 1987 (D. Swinbanks 1987; F. Makino 1987). Two earlier black hole sources, namely Cen X–2 (R. Francey 1971) and MX 1353–64 (T. H. Markert et al. 1979), were also reported from the same sky location as GS 1354–64. According to S. Kitamoto et al. (1990), these sources are likely to be the same object. Dynamical studies later confirmed GS 1354–64 as a black hole with a mass of  $M_{\text{BH}} = 7.9 \pm 0.5 M_{\odot}$  and an orbital period of  $P_{\text{orb}} = 2.54$  days (J. Casares et al. 2009). J. Casares et al. (2004) identified the binary companion as a G0–5 III star with a mass of  $1.1 \pm 0.1 M_{\odot}$ . Furthermore, J. Casares et al. (2009) constrained the distance and inclination angle of GS 1354–64 to be  $\geq 25$  kpc and  $\sim 75^{\circ}$ , respectively. From a model-dependent study of the reflection-dominated hard-state spectrum during the 2015 outburst, A.M. El-Batal et al. (2016) estimated the black hole spin and inclination angle to be  $a_k = 0.98$  and  $i = 75^{\circ}$ , respectively. Using HEASARC column density tool, A.M. El-Batal et al. (2016) adopted a hydrogen column density of  $N_{\text{H}} = 7 \times 10^{21} \text{ cm}^{-2}$  for their spectral analysis. A similar range of  $N_{\text{H}} \sim (5\text{--}9) \times 10^{21} \text{ cm}^{-2}$  is also reported by P.W.N. Kalberla et al. (2005) from the Galactic HI survey within a  $1^{\circ}$  radius of the location of GS 1354–64.

Recently, on 2025 December 25 (MJD 61034), *MAXI*/GSC detected a new outburst of the source (H. Negoro et al. 2025). This detection was subsequently confirmed by several missions across multiple wavelengths, ranging from radio and optical to X-rays. O.K. Adegoke et al. (2026) reported the detection of relativistic reflection features based on a preliminary analysis of *NuSTAR* data. Based on the evolution of the *MAXI*/GSC count rates in the soft and hard energy bands, H. Negoro et al. (2026) reported a transition in the spectral nature of the source from the hard to the soft state on 2026 January 19 (MJD 61059). During the outburst, a broad signature of Fe emission line with *XRISM* (H. Liu et al. 2026) and detection of polarization with *IXPE* (S. Ravi et al. 2026) are also reported.

In this *paper*, we present the first results on the spectral and temporal properties of GS 1354–64 during its 2025–26 non-conventional outburst. We analyze archival data from multiple satellites, namely *MAXI*, *NuSTAR*, and *Insight-HXMT*, covering the period from the ini-

tial phase of the outburst up to 2026 February 19. The paper is organized as follows: §2 describes the observations, data reduction, and analysis methods. In §3, we present the results of our detailed spectral and timing analyses, while §4 discusses our findings and presents the conclusions.

## 2. OBSERVATION AND DATA ANALYSIS

We study the recent outburst of the Galactic transient BH GS 1354–64 using on-demand data from *MAXI*/GSC and archival data from the *NuSTAR*/FPMA and *Insight-HXMT*/LE, ME, and HE instruments. We follow standard data reduction procedures for both *NuSTAR*<sup>5</sup> and *Insight-HXMT*<sup>6</sup> satellites. The *NuSTAR* data are extracted using the online platform SciServer<sup>7</sup>, employing the latest version (v6.36) of the HEASoft package provided by HEASARC. The *Insight-HXMT* data analysis is performed locally using the satellite software package within HEASoft (v6.34) after downloading the archival data.

### 2.1. *MAXI*

To study the outburst profile and hardness ratio evolution between 2025 December 25 (MJD 61034) and 2026 February 19 (MJD 61090), *MAXI*/GSC daily-averaged fluxes in the soft (2–6 keV) X-ray (SXR) and hard (6–20 keV) X-ray (HXR) bands are downloaded from the *MAXI* RIKEN on-demand website<sup>8</sup>. The ratio of the HXR to SXR flux is defined as the hardness ratio (HR), while the 2–20 keV flux is referred to as the total X-ray (TXR) flux.

### 2.2. *NuSTAR*

The *NuSTAR* (F.A. Harrison et al. 2011) TOO observations of 2026 Jan 13 (ObsID 91201302002), Jan 21 (ObsID 91201302004), Jan 24 (91201302006), Jan 30 (ObsID 91202308002), Feb 11 (91202311002) and Feb 11 (91202311004) are reduced using the *NuSTARDAS* software (v2.1.4). Cleaned event files are produced with the *nupipeline* task using the latest calibration files. Source spectra and light curves (in 10 s, 1 s, 0.01 s bins) are extracted from a circular region of  $50''$  radius centered at the source coordinates, while corresponding background files are extracted from an annular region ( $180'' - 240''$ ) defined using DS9. The standard *nuproducts* task is used to generate source spectra, auxiliary response files, and response matrix files. To improve signal-to-noise ratio, we further rebinned spectra using *GRPPHA* task to have at least 100 counts per bin.

<sup>5</sup> <https://heasarc.gsfc.nasa.gov/docs/nustar/analysis>

<sup>6</sup> <http://hxmtcn.ihep.ac.cn/analysis.jhtml>

<sup>7</sup> <https://www.sciserver.org>

<sup>8</sup> <https://maxi.riken.jp/mxondem>

### 2.3. *Insight-HXMT*

We study publicly available archival data of 37 observations of *Insight-HXMT* (S. Zhang et al. 2014; S.-N. Zhang et al. 2020) in between 2026 Jan 18 (MJD 61058.18) to Feb 08 (MJD 61079.34) are extracted using latest calibration files (v2.08) to study detailed temporal and spectral properties of the source. We generate 1 s and 0.01 s time binned light curves in different energy bands of LE (2 – 4 keV, 4 – 10 keV, 2 – 10 keV), ME (8 – 30 keV, 10 – 30 keV), and HE (27 – 150 keV). For the spectral analysis, we used data in default energy bands data, which covers maximum energy band of LE, ME, HE instruments. The data extraction for generating light curves and spectral files was performed using `hpipeline` pipeline within the `HEASoft` software package (v.6.34) from HEASARC. To improve signal-to-noise ratio, we also rebinned spectra to ensure at least 50 counts per bin using the `GRPPHA` task.

### 2.4. Data Analysis

To search for the key temporal feature, namely QPOs, we generated Fast Fourier transform power density spectra (PDS) using 0.01 s time-binned light curves from the *NuSTAR* and *Insight-HXMT* satellites. We used the `XRONOS` task `powspec` (part of the `HEASoft` software package) with `norm=2`, which produces PDS in units of squared fractional rms variability without white-noise subtraction. To determine the QPO parameters: centroid frequency ( $\nu_{QPO}$ ), full width at half maximum (FWHM), and normalized power, the PDS were fitted using a combination of Lorentzian and constant models.

The broadband *Insight-HXMT* spectrum in the 2–60 keV energy range after combining data from LE (2–8 keV), ME (8–30 keV), and HE (27–60 keV), was fitted with the following models – M1: `constant*tbabs(diskbb+powerlaw)`, M2: `constant*tbabs(thcomp*diskbb)`, and M3: `constant*tbabs(diskbb+relxill)`. Similarly, the 3–70 keV *NuSTAR*/FPMA spectrum was fitted using the same three model combinations. Here, to obtain statistically acceptable fits, an additional Gaussian component was required in model combination M1 and M2. For spectral fit, we used fixed value of the hydrogen column density  $N_H = 7 \times 10^{21} \text{ cm}^{-2}$  for absorption model `tbabs`.

## 3. RESULTS

The detailed temporal and spectral properties during the initial phase of the outburst of the Galactic transient BH GS 1354–64 are studied using data from three satellite instruments, namely *MAXI*/GSC, *NuSTAR*/FPMA, and *Insight-HXMT*/LE, ME, and HE. The *MAXI* data are used to investigate the daily evolution of the outburst profile and hardness ratios, while the *NuSTAR* and *Insight-HXMT* data are used for detailed temporal and spectral studies of the source. In the following sub-

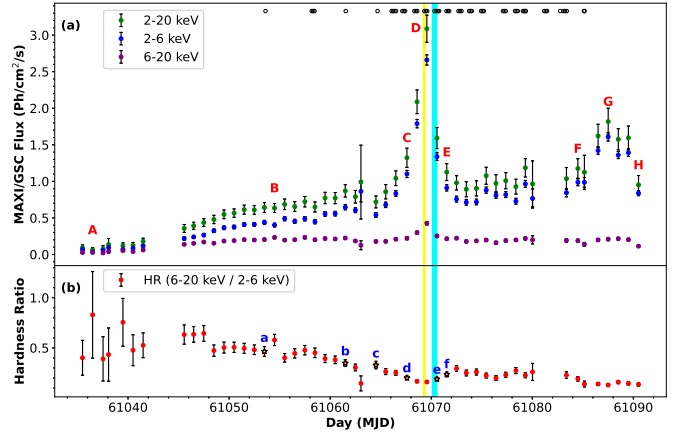


**Figure 1.** Variation of (a) *MAXI*/GSC fluxes in the SXR (2–6 keV), HXR (6–20 keV), and TXR (2–20 keV) energy bands, and (b) the hardness ratio (HR), defined as the ratio of HXR to SXR fluxes. The yellow and cyan shaded regions indicate the observation periods of the *Insight-HXMT* and *NuSTAR* satellites, respectively, for which detailed spectral analyses are performed. The points A–H in the upper panel mark different stages of the HID (see Fig. 2), while the points labeled (lower panel) a–f denote the MJDs corresponding to different stages of the QPO evolution (see Fig. 4).

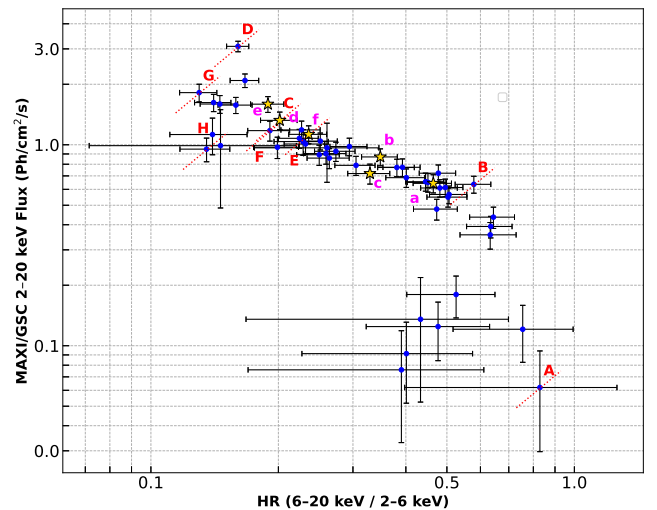


**Figure 2.** The *MAXI*/GSC hardness–intensity diagram (HID) from 2025 December 27 (MJD 61036) to 2026 February 19 (MJD 61090) is shown. The dashed-line points A, E, and D indicate the start, end, and peak of the initial phase of the outburst, respectively, whereas the dotted-line points B and C mark the onset of strong inflow in the SXR, triggering an X-ray flare and the end of the flare, respectively. The star-shaped points a–f denote different evolutionary phases of the QPO, as indicated in Fig. 4. Both X- and Y-axes are shown on logarithmic scales.

sections, we present our analysis results based on observations from these multi-mission satellite instruments.

### 3.1. Outburst Profile and Hardness-Intensity Diagram

*MAXI* monitored the new outburst of GS 1354–64 on an approximately daily basis, starting from its detection on 2025 December 25 (MJD 61034). In Fig. 1(a), we present the evolution of the daily averaged fluxes in the soft (2–6 keV), hard (6–20 keV), and total (2–20 keV) X-ray bands of the *MAXI*/GSC from 2025 December 27 (MJD 61036) to 2026 February 19 (MJD 61090). These three energy bands are hereafter referred to as SXR, HXR, and TXR, respectively. The points A–H mark the start, end, or transitions between important evolutionary phases of the 2025–26 outburst. The yellow and cyan shaded regions indicate the soft-state observation periods of *Insight*-HXMT and *NuSTAR*, respectively, for which detailed spectral analyses were performed to estimate the spin and inclination angle of the source. In Fig. 1(b), we show the evolution of the hardness ratio (HR), defined as the ratio of the HXR to SXR fluxes. The source exhibits strong low-frequency QPOs and their temporal evolution. The points a–f mark key phases of the QPO frequency evolution, the details of which are discussed in the following subsection.

The initial phase of the ongoing 2025–26 outburst shows a slow rise with an unusual short-duration ( $\sim 3$  days) X-ray flare, reaching a peak flux of  $\sim 1.4$  Crab (at point D on 2026 Jan. 29; MJD 61069) in the 2–20 keV band of the GSC. A rebrightening episode lasting for  $\sim 6$  days, with a peak flux of  $\sim 0.8$  Crab (at point G on 2026 Feb. 16; MJD 61087) in the same energy band of *MAXI*/GSC, is observed after a gap of  $\sim 13$  days.

The higher HR up to point B (2026 Jan. 14; MJD 61054) indicates that the source was likely in the LHS between points A and B. Owing to an increasing trend in the SXR flux, a declining trend in HR is observed during the period between points B and C (2026 Jan. 14 to 24; MJD 61054–61067). We identify this phase as the HIMS. The interval between points C and E (2026 Jan. 24 to 27; MJD 61067–61069) marks the short X-ray flare, with the CD and DE branches representing the rising and declining phases of the flare, respectively. During these phases, a rapid rise and fall in the SXR-band flux is observed with little variation in the HXR band. This behavior implies a sudden inflow of thermally cooler Keplerian matter from the outer accretion disk, i.e., from the pile-up radius ( $X_p$ ). During this primary flare phase (C–E), the source likely entered the softer spectral states (HSS or SIMS). The HR remains at a lower value during the flaring phase, indicating a softening of the spectral nature of the source. Subsequently, during the period E–F, the fluxes in both hard and soft bands, as well as the HR, remain nearly constant for  $\sim 16$  days. We identify this phase of the outburst as a probable SIMS. The rebrightening of the X-ray flare (F–H) is observed between 2026 Feb. 13 and 19

(MJDs 61084–61090). The HR is further reduced during this phase, indicating continued spectral softening. A detailed spectral study to confirm the above spectral classification in different phases of the outburst is being carried out and will be published elsewhere.

The HID, i.e., the variation of HR with TXR shown in Fig. 2, displays the canonical rising hard and intermediate spectral branches characteristic of a classical (type-I) outburst of transient BH-XRBs (see, e.g., [A. Nandi et al. 2012](#)). The vertically rising branch A–B indicates the signature of the LHS (rising), while the BC segment corresponds to the HIMS (rising). The flare period C–D–E reflects a softer spectral nature of the source. Interestingly, the HR in the declining flare branch (D–E) follows a path similar to that of the rising flare branch (C–D), but in the reverse direction. The HR variation during the subsequent nearly constant flux phase (E–F) shows a tendency toward the SIMS, which is further supported by the observed QPO evolution. A further decrease in HR is observed during the F–H period, which corresponds to the flare rebrightening or second flare phase, indicating that the spectra become even softer during this stage of the outburst.

### 3.2. Evolution of Low Frequency QPOs

A strong signature of low-frequency QPOs is observed in the PDS of each *NuSTAR* and *Insight*-HXMT data, except during the softer phase of the outburst (2026 Jan 28–29; MJD 61068.33–61069.60), which covers part of the primary X-ray flare. The details of the Lorentzian model fitted QPO frequency ( $\nu$ ), Q-value ( $\nu/\text{FWHM}$ ), fractional rms ( $\% \text{ rms} = 100 \sqrt{\pi \times \text{power} \times \text{FWHM}/2}$ ), and significance ( $\sigma$ , defined as the ratio of the norm to its negative error of the Lorentzian model fitted QPOs) are listed in Table 1.

A monotonic evolution of the QPO frequencies is observed during the initial phase of the outburst. In the very first *NuSTAR* observation on 2026 Jan 13 (MJD 61053.61), a type-C QPO at 0.073 Hz is detected. In the follow-up observations with *NuSTAR* and *Insight*-HXMT, the QPO frequencies increase monotonically up to  $\sim 4$  Hz at point C in Fig. 1(a) (2026 Jan 27; MJD 61067.41). After that, no QPOs are detected for the next  $\sim 2$  days, which includes the peak of the first flare. The QPO reappears in the declining phase of the flare on 2026 Jan 30 (MJD 61070.33). Subsequently, it shows a monotonically decreasing trend over the next  $\sim 1.5$  days, until 2026 Jan 31 (MJD 61071.78). During this shorter evolution phase, the QPO frequency rapidly decreases from 6.14 Hz to 3.26 Hz, a behavior generally observed during the canonical declining phase of classical outbursts in transient BH-XRBs. This type of monotonically decreasing trend in the QPO frequency immediately after an increasing trend, or during the rising phase of an outburst, is uncommon. However, a similar evolution was observed in Swift J1727.8-1613 during its recent discovery outburst ([D. Debnath et al. 2025](#)).

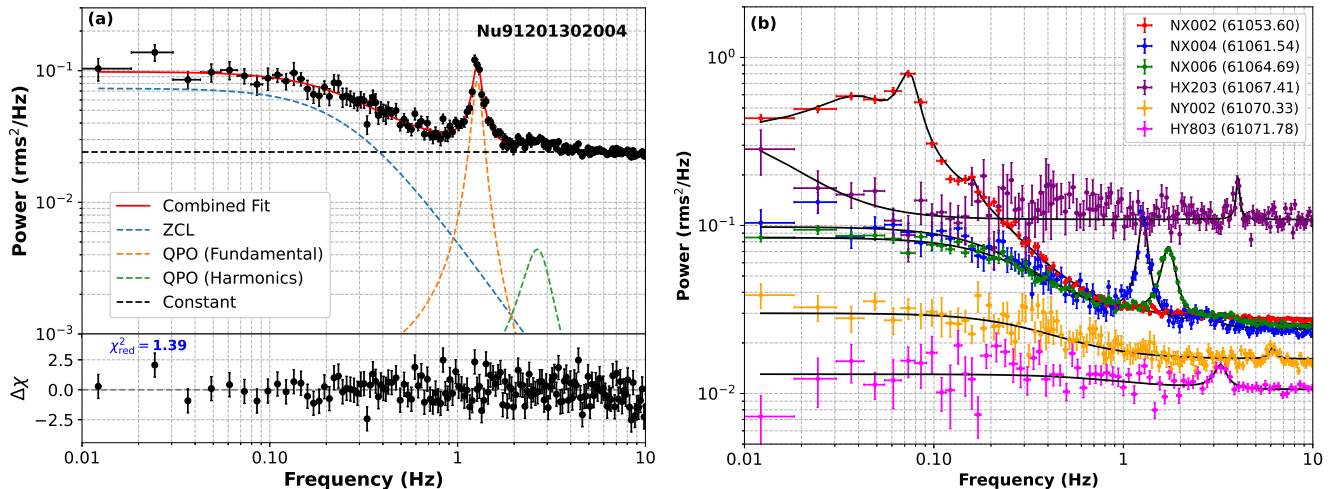


**Figure 3.** (a) Power Density Spectrum of *NuSTAR* data (ObsID 91201302004), fitted with a combination of three Lorentzian components (one zero-centred and two QPO-centred) and a constant model. (b) PDS of six observations selected from six different evolutionary phases, as marked by points a–f in Fig. 4. For clarity, the power in the final observation shown in panel (b) has been divided by a factor of 10.

After that, a non-evolving, sporadic nature of the QPOs is observed for the next  $\sim 13$  days, until 2026 Jan 14 (MJD 61085.17). This type of sporadic QPO behavior is commonly seen during the SIMS of transient BH-XRB outbursts. For instance, similar non-evolving, sporadic QPOs were observed during the SIMS of the recent outburst of Swift J1727.8–1613 (D. Debnath et al. 2025) and the 2010–11 outburst of GX 339–4 (A. Nandi et al. 2012).

We further study the monotonic evolution (both increasing and decreasing) of the QPO frequencies using the propagating oscillatory shock (POS) model. This approach allows us to understand the properties of the shock wave, whose oscillation is to be considered the origin of the observed low-frequency QPOs (see, e.g., S.K. Chakrabarti et al. 2008; D. Debnath et al. 2010, 2025). In Fig. 4, we show the evolution of the QPOs fitted with the POS model. The shock is observed to move inward (from  $1230 r_s$  to  $211 r_s$ , where  $r_s$  is the Schwarzschild radius) during the monotonically increasing phase of the QPOs, marked by points a – d. Conversely, during the short monotonically decreasing phase of the QPO frequency (region between e – f), the shock recedes from  $151 r_s$  to  $226 r_s$ .

Based on the POS model-fitted shock parameters, such as the shock strength and velocity, we classify the evolution of the QPO frequency into four stages: (i) a–b, (ii) b–c, (iii) c–d, and (iv) e–f. Faster shock motion is observed during phases (i) and (iv). In these four phases, the shock moves inward or outward with velocities of  $\sim 2, 0.2, 0.25,$  and  $0.8 \text{ m s}^{-1}$ , respectively. The strong shock (compression ratio  $R = 4$ ) at point a weakens to  $R \simeq 1$  by the last day of the increasing QPO phase at point d. During the receding phase (iv), the

shock remains weak, with only a very slight increase in strength.

During the rising phase, due to the slowing down of the shock movement between points b and c ( $\sim 3$  days), only a small increase in the QPO frequency (1.46–1.73 Hz) is observed. After that, over a roughly similar time interval between points c and d, a sharp increase in the QPO frequency from 1.73 to 4 Hz is observed. During this rapid QPO increasing phase, although the shock velocity remains nearly the same, the rapid weakening of the shock strength ( $R$  reduced from  $\sim 1.54$  to 1) is likely to be the primary cause of the sharp rise in the QPO frequency.

### 3.3. Spectral Modeling: On the nature of Spin

Broadband spectra using LE (2–8 keV), ME (8–29 keV), and HE (29–60 keV) data from *Insight-HXMT* and *NuSTAR* are used for the spectral analysis. The primary goal is to understand the nature of the source during the unconventional flare phase. We selected the flare-peak data from *Insight-HXMT* (ObsID P081404800601 on MJD 61069.32; hereafter referred to as SPEC1) with an exposure of  $\sim 2$  ks and the nearest *NuSTAR* observation (ObsID 91202308002 on MJD 61070.33; hereafter referred to as SPEC2) with an exposure of  $\sim 12$  ks, as marked by the yellow and cyan shaded regions in Fig. 1. In Fig. 5, we show both spectra fitted with three different models (see §2.4). A strong signature of relativistic reflection is observed in both observations.

To understand the overall spectral nature of the source during the short flare-peak phase, we first fitted both spectra with the phenomenological model M1, comprising a thermal disk blackbody plus a nonthermal powerlaw component. Although model M1 fits

**Table 1.** Model Fitted QPO Results

| Sr. | ObsID               | UT    | MJD <sub>Avg</sub> | $\nu_{QPO}$               | Q    | rms(%) | $\sigma$ |
|-----|---------------------|-------|--------------------|---------------------------|------|--------|----------|
| 1   | NX2002 <sup>a</sup> | 01/13 | 61053.61           | $0.073^{+0.003}_{-0.001}$ | 3.21 | 13.7   | 7.16     |
| 2   | HX0101              | 01/18 | 61058.18           | $0.26^{+0.01}_{-0.02}$    | 8.13 | 14.9   | 3.31     |
| 3   | HX0102              | 01/18 | 61058.32           | $0.28^{+0.01}_{-0.01}$    | 3.56 | 18.3   | 4.88     |
| 4   | HX0103              | 01/18 | 61058.44           | $0.28^{+0.01}_{-0.02}$    | 4.40 | 14.9   | 2.76     |
| 5   | NX2004 <sup>b</sup> | 01/21 | 61061.54           | $1.46^{+0.01}_{-0.01}$    | 3.93 | 15.9   | 23.9     |
| 6   | NX2006 <sup>c</sup> | 01/24 | 61064.69           | $1.73^{+0.01}_{-0.01}$    | 5.28 | 15.6   | 22.4     |
| 7   | HY0101              | 01/26 | 61066.08           | $2.33^{+0.04}_{-0.05}$    | 7.68 | 20.0   | 4.28     |
| 8   | HY0102              | 01/26 | 61066.22           | $2.59^{+0.03}_{-0.03}$    | 7.33 | 21.1   | 5.86     |
| 9   | HY0103              | 01/26 | 61066.37           | $2.72^{+0.03}_{-0.03}$    | 11.1 | 19.4   | 4.79     |
| 10  | HY0104              | 01/26 | 61066.53           | $2.77^{+0.03}_{-0.04}$    | 10.5 | 18.6   | 3.65     |
| 11  | HX0201              | 01/27 | 61067.14           | $3.36^{+0.09}_{-0.09}$    | 4.87 | 21.4   | 4.54     |
| 12  | HX0202              | 01/27 | 61067.28           | $3.53^{+0.12}_{-0.10}$    | 3.68 | 23.4   | 5.13     |
| 13  | HX0203 <sup>d</sup> | 01/27 | 61067.41           | $3.92^{+0.10}_{-0.06}$    | 12.9 | 19.7   | < 4      |
| 14  | HY0301              | 01/28 | 61068.33           | —                         | —    | —      | —        |
| 15  | HY0302              | 01/28 | 61068.49           | —                         | —    | —      | —        |
| 16  | HY0303              | 01/28 | 61068.61           | —                         | —    | —      | —        |
| 17  | HY0601              | 01/29 | 61069.32           | —                         | —    | —      | —        |
| 18  | HY0602              | 01/29 | 61069.47           | —                         | —    | —      | —        |
| 19  | HY0603 <sup>e</sup> | 01/29 | 61069.60           | —                         | —    | —      | —        |
| 20  | NY8002              | 01/30 | 61070.33           | $6.14^{+0.16}_{-0.20}$    | 12.4 | 14.3   | < 4      |
| 21  | HY0701              | 01/30 | 61070.52           | $6.16^{+0.30}_{-0.28}$    | 5.35 | 14.3   | < 3      |
| 22  | HY0702              | 01/30 | 61070.67           | $5.07^{+0.30}_{-0.32}$    | 4.00 | 17.3   | 3.19     |
| 23  | HY0801              | 01/31 | 61071.51           | $3.63^{+0.05}_{-0.05}$    | 8.32 | 20.2   | 4.85     |
| 24  | HY0802              | 01/31 | 61071.66           | $3.50^{+0.04}_{-0.04}$    | 11.4 | 17.8   | 4.61     |
| 25  | HY0803 <sup>f</sup> | 01/31 | 61071.78           | $3.26^{+0.11}_{-0.11}$    | 5.54 | 19.4   | 3.24     |
| 26  | HY0901              | 02/01 | 61072.70           | $3.64^{+0.05}_{-0.06}$    | 6.66 | 21.1   | 4.38     |
| 27  | HY0902              | 02/01 | 61072.84           | $3.79^{+0.07}_{-0.07}$    | 7.11 | 20.2   | 3.78     |
| 28  | HY0903              | 02/01 | 61072.99           | $3.61^{+0.06}_{-0.06}$    | 7.20 | 21.1   | 4.08     |
| 29  | HY1001              | 02/02 | 61073.75           | $3.16^{+0.06}_{-0.06}$    | 6.13 | 20.2   | 4.81     |
| 30  | HY1002              | 02/02 | 61073.90           | $3.32^{+0.06}_{-0.06}$    | 5.74 | 23.1   | 4.55     |
| 31  | HY1101              | 02/03 | 61074.93           | $3.42^{+0.04}_{-0.04}$    | 9.66 | 17.9   | 4.13     |
| 32  | HY1102              | 02/04 | 61075.08           | $3.61^{+0.07}_{-0.07}$    | 9.34 | 16.7   | < 3      |
| 33  | HY1103              | 02/04 | 61075.21           | $4.00^{+0.09}_{-0.08}$    | 8.98 | 20.8   | 3.01     |
| 34  | HY1301              | 02/06 | 61077.10           | $4.59^{+0.12}_{-0.12}$    | 8.43 | 16.9   | < 3      |
| 35  | HY1302              | 02/06 | 61077.23           | $4.46^{+0.76}_{-0.32}$    | 3.10 | 20.5   | < 3      |
| 36  | HY1401              | 02/07 | 61078.30           | $4.25^{+0.23}_{-0.18}$    | 6.01 | 19.4   | < 3      |
| 37  | HY1402              | 02/07 | 61078.44           | $4.33^{+0.36}_{-0.34}$    | 2.78 | 24.3   | 3.27     |
| 38  | HY1403              | 02/07 | 61078.56           | $3.86^{+0.10}_{-0.11}$    | 9.23 | 19.4   | < 3      |
| 39  | HY1901              | 02/08 | 61079.07           | $4.75^{+0.22}_{-0.18}$    | 5.07 | 19.8   | 3.20     |
| 40  | HY1903              | 02/08 | 61079.34           | $5.02^{+0.11}_{-0.09}$    | 8.51 | 7.07   | 3.00     |
| 41  | NZ1002              | 02/11 | 61082.76           | $4.67^{+0.05}_{-0.04}$    | 8.22 | 7.67   | 7.33     |
| 42  | NZ1004              | 02/14 | 61085.17           | $5.81^{+0.13}_{-0.12}$    | 12.6 | 4.51   | < 4      |

NX=9120130, NY=9120230, NZ=9120231, HX=P08140470, HY=P08140480 are pre-fixes of the NuSTAR and HXMT observation IDs. UT in dd/mm format and  $\nu_{QPO}$  in Hz. Q ( $=\nu_{QPO}/FWHM$ ), % of rms, and significance ( $\sigma$ ) define nature of the QPOs. Note that some of the HXMT observations show  $\sigma \sim 3$  due to less statistics.

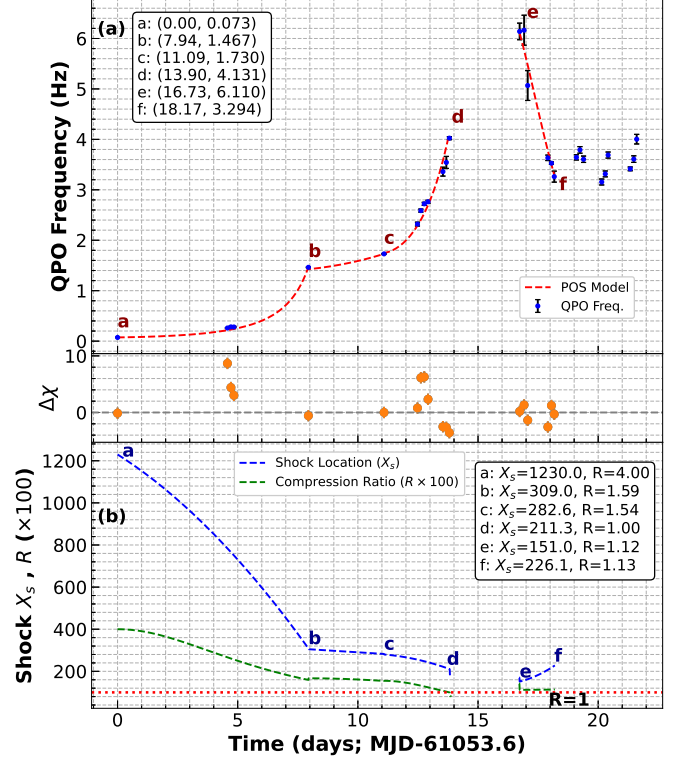


**Figure 4.** (a) Variations of the observed QPO frequencies with time (in days) during the initial phase of the outburst, along with the best-fitted POS model (dashed curve), are shown. (b) Variations of the shock location (in units of the Schwarzschild radius,  $r_s$ ) and the shock compression ratio ( $R$ ) are presented. The variation of the model-fitted  $\Delta\chi$  is shown in the middle panel. Here, points a-f mark the start, end, or major transition phases of the evolution. The monotonically increasing and decreasing trends of the QPO frequencies during periods a-d and e-f, respectively, are similar to the rising and declining phases of canonical outbursts of transient BH-XRBs, while the sporadic nature of the QPOs beyond point f resembles that observed during the SIMS.

SPEC1 reasonably well, it fails to adequately describe the broader energy band (3–70 keV) higher resolution *NuSTAR* spectrum, particularly above  $\sim 50$  keV. A broad Fe emission line at  $\sim 6.5$  keV is also evident in the *NuSTAR* spectrum. Higher disk temperatures ( $T_{in} > 1.2$  keV) and steep photon indices ( $\Gamma > 2.4$ ) in both observations indicate that the source was in a softer (HSS and SIMS) spectral state.

We then replaced the nonthermal powerlaw component with the physical thermal Comptonization model `thcomp`. This provides a better understanding of the ‘hot’ corona, which is responsible for producing the non-thermal hard photons. Model M2 is used to fit both spectra. But an additional `gaussian` component for the Fe emission line is required to achieve a satisfactory fit in SPEC2. It is to be noted that the physical `thcomp`

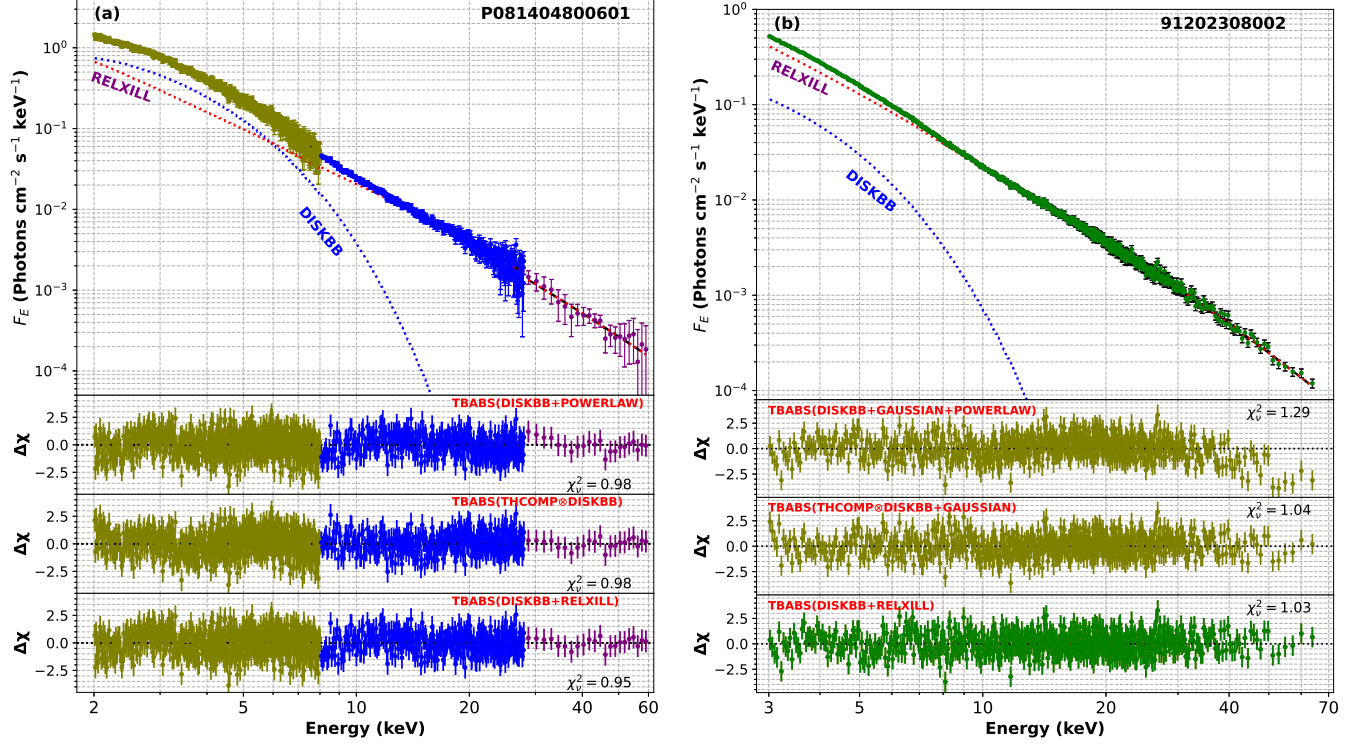


**Figure 5.** Broadband spectra of (a) *Insight-HXMT* (ObsID P081404800601; MJD 61069.32; SPEC1) and (b) *NuSTAR/FPMA* (ObsID 91202308002; MJD 61070.33; SPEC2), close to the first flare peak, are fitted with different combinations of spectral models M1, M2 and M3 (see §2.4). The lower panels show the residuals, expressed as the variations of the model-fitted  $\Delta\chi$ , for the corresponding models (marked in the insets). See text for details.

**Table 2.** Model Fitted Spectral Parameters with Different Components of Respective Models

| <sup>1</sup> TBABS(DISKBB + POWERLAW) |                        |                    | /                      |                        |                        | <sup>4</sup> TBABS(DISKBB + GAUSSIAN + POWERLAW) |              |                    |                        |                        |              |
|---------------------------------------|------------------------|--------------------|------------------------|------------------------|------------------------|--|--------------|--------------------|------------------------|------------------------|--------------|
| ObsID                                 | $kT_{in}$              | $N_{DBB}$          | $\Gamma$               | $N_{PL}$               | $\chi^2/DOF$           |  |              |                    |                        |                        |              |
| HY601 <sup>1</sup>                    | $1.23^{+0.01}_{-0.01}$ | $264^{+19}_{-19}$  | $2.41^{+0.02}_{-0.02}$ | $5.43^{+0.39}_{-0.38}$ | 1037/1056              |  |              |                    |                        |                        |              |
| NY002 <sup>4</sup>                    | $1.24^{+0.03}_{-0.02}$ | $53^{+6.4}_{-6.3}$ | $2.65^{+0.01}_{-0.01}$ | $10.1^{+0.28}_{-0.27}$ | 808/626                |  |              |                    |                        |                        |              |
| <sup>2</sup> TBABS(THCOMP⊗DISKBB)     |                        |                    | /                      |                        |                        | <sup>5</sup> TBABS(THCOMP⊗DISKBB + GAUSSIAN)     |              |                    |                        |                        |              |
| ObsID                                 | $\Gamma_\tau$          | $kT_e$             | $Cov_{frac}$           | $kT_{in}$              | $N_{DBB}$              | $\chi^2/DOF$                                     | $F_{THCOMP}$ | $F_{DBB}$          | FR                     |                        |              |
| HY601 <sup>2</sup>                    | $2.49^{+0.03}_{-0.03}$ | < 30               | $0.48^{+0.04}_{-0.04}$ | $0.99^{+0.02}_{-0.02}$ | $1110^{+99}_{-85}$     | 1030/1056  | 8.1          | 5.8                | 1.4                    |                        |              |
| NY002 <sup>5</sup>                    | $2.50^{+0.03}_{-0.03}$ | $41^{+9}_{-8}$     | $0.72^{+0.07}_{-0.06}$ | $0.95^{+0.02}_{-0.02}$ | $840^{+64}_{-55}$      | 651/625  | 7.5          | 3.4                | 2.2                    |                        |              |
| <sup>3</sup> TBABS(DISKBB+RELXILL)    |                        |                    |                        |                        |                        |  |              |                    |                        |                        |              |
| ObsID                                 | $kT_{in}$              | $N_{DBB}$          | $a_k$                  | $i$                    | $\Gamma$               | $\log \xi$                                       | $A_{Fe}$     | $E_{cut}$          | $refl_{frac}$          | $N_{RELXILL}$          | $\chi^2/DOF$ |
| HY601 <sup>3</sup>                    | $1.23^{+0.01}_{-0.01}$ | $293^{+11}_{-10}$  | $0.998^{+p}_{-0.002}$  | $64.8^{+2.0}_{-2.1}$   | $2.46^{+0.05}_{-0.04}$ | $2.99^{+0.07}_{-0.13}$                           | < 0.65       | $200^f$            | $3.78^f$               | $0.33^{+0.01}_{-0.01}$ | 1004/1053    |
| NY002 <sup>3</sup>                    | $1.17^{+0.02}_{-0.03}$ | $90^{+5.1}_{-4.7}$ | $0.998^{+p}_{-0.001}$  | $68.4^{+1.6}_{-1.8}$   | $2.40^{+0.02}_{-0.03}$ | $3.69^{+0.24}_{-0.42}$                           | < 5.0        | $65^{+3.8}_{-4.2}$ | $0.38^{+0.02}_{-0.04}$ | $0.45^{+0.01}_{-0.01}$ | 642/624      |

HY=P0814048006 and NY=91202308 are the pre-fixes of the Insight-HXMT (H) and NuSTAR (N) observation IDs.

<sup>f</sup> Unable to constrain error limits, model parameters are kept frozen at their best fitted values.

Fixed values of TBABS:  $N_H = 7 \times 10^{21} \text{ cm}^{-2}$

RELXILL: Index1, Index2= 9,  $R_{br} = 15$ ,  $R = -1$ , and  $R_{out} = 400$  are used.

Units of  $kT_{in}$ ,  $kT_e$ ,  $E_{cut}$  in keV;  $R_{br}$  in ISCO radius;  $R_{out}$  in Gravitational radius  $r_g = GM/C^2$ .

Thermal DISKBB and nonthermal THCOMP fluxes  $F_{DBB}$ , and  $F_{THCOMP}$  are in  $10^{-9} \text{ erg cm}^{-2} \text{ s}^{-1}$ .

FR is the ratio of the nonthermal to thermal fluxes.

Note, model fitted parameter errors are the average values of the  $1\sigma \pm$  errors and spin upper limit is pegged to the hard bound.

model is quite successful in fitting the nonthermal continuum, including the feature above 50 keV. An increase in corona temperature ( $kT_e$ ), and the covering fraction of the thermal seed photons in SPEC2 indicates that the corona becomes relatively hotter, with a possible increase in its size and optical depth. Furthermore, we note that the spectrum becomes slightly harder even within the softer state, as indicated by an increase in the flux ratio (FR), defined as the ratio of nonthermal to thermal flux. Note that due to the lower spectral resolution and lower exposure of HXMT, no prominent Fe line is observed in SPEC1.

Finally, to estimate intrinsic source parameters such as spin and inclination angle, and to understand the spectral nature from a physical perspective, both spectra were fitted using the relativistic reflection model `relxill`. For SPEC2, this model did not require an additional Gaussian Fe line profile. The lower disk temperature ( $T_{in}$ ) and photon index ( $\Gamma$ ) indicate that the source moved toward a slightly harder spectral state during SPEC2. The higher high-energy cutoff ( $E_{cut}$ ) suggests that the corona size may have been smaller during SPEC1. A higher relativistic reflection fraction in the SPEC1 is also consistent with it. The source spin is estimated to be  $a_k = 0.998_{-0.002}^{+p}$  and  $0.998_{-0.001}^{+p}$ , at inclination angles  $i = (65.2_{-2.1}^{+2.4})^\circ$  and  $(68.4_{-1.8}^{+1.6})^\circ$  for SPEC1 and SPEC2, respectively, from model M3. The high spin values indicate that the source is a maximally rotating Kerr black hole. The estimated spin and inclination angle of the source are consistent with earlier results reported by A.M. El-Batal et al. (2016) and J. Casares et al. (2009).

#### 4. DISCUSSION AND CONCLUDING REMARKS

The initial phase of the 2025–26 outburst of the Galactic transient BH GS 1354-64 is studied using data from *MAXI/GSC*, *Insight-HXMT*, and *NuSTAR*. The source exhibited an unconventional outburst profile, although it began with a common trend of slow-rise. The outburst included a short X-ray flare of  $\sim 3$  days, followed by a re-brightening after  $\sim 13$  days. The maximum fluxes during the peaks of the primary and secondary flares were observed to be 1.4 Crab and 0.8 Crab, respectively. Note that the outburst is still ongoing at a flux level similar to that of the plateau phase (E–F).

The on-demand data from *MAXI/GSC* were used to study the outburst profile of the source. The daily-averaged GSC fluxes in the soft (2–6 keV; SXR), hard (6–20 keV; HXR), and total (2–20 keV; TXR) X-ray bands, along with their ratio defined as the hardness ratio ( $HR = HXR/SXR$ ), allow us to characterize the spectral behavior of the source during the 2025–26 outburst. From the evolution of the fluxes in different energy bands, it is evident that the outburst was primarily driven by thermal soft photons, as the TXR closely followed the trend of the SXR, while the HXR flux remained roughly constant throughout the outburst.

The points A–H in Fig. 1 mark important evolutionary phases of the outburst profile and HR. In the early phase of the outburst, between points A and B, the HR remained roughly constant at higher values. The vertical branch in the HID (Fig. 2) during this phase indicates that the source was in the LHS. The phase between points B and C is defined as the HIMS, as a decreasing trend in the HR with an increase in the SXR is observed. During the primary flare period (between points C–D–E), a nonconventional evolution of the HR is observed. The declining flare branch (D–E) follows the same returning path as the rising flare branch (C–D). The source was found to be in its softest phase on the peak day (point D) of the primary flare, as indicated by the lowest HR. After this, the source remained roughly constant in both X-ray intensity and HR between points E and F. Starting from point F, the HR decreased and remained at lower values during the second flare (between points F–G–H). Although the timescales and physical processes associated with GS 1354-64 (a BH-XRB) and pulsars (neutron stars) are different, the HR and flux plateau phase (E–F) between the two flares appears similar to the bridge between the on- and off-pulse phases of a pulsar.

The physical origin of the two intense, short-duration flares may be attributed to a sudden increase in the supply of high-viscosity Keplerian matter into the disk from a temporary reservoir at the pile-up radius  $X_p$ , leading to a short-term enhancement in the SXR rate. A rapid decline in TXR is observed immediately after the first flare. However, the plateau phase between the two flares indicates a fresh supply of matter from  $X_p$  following the initial decay of the first flare, which likely triggered the second flare of the outburst. From the evolution of the outburst profile, HR, and HID, it appears that the 2025–26 outburst of GS 1354–64 does not correspond to a canonical type-I or type-II outburst. A more detailed spectral study of the entire 2025–26 outburst of GS 1354–64 will be carried out and presented elsewhere.

A strong signature of low-frequency QPOs is observed in both *Insight-HXMT* and *NuSTAR* observations throughout the outburst, except during the initial  $\sim 2$  days of the primary X-ray flare. Prior to their disappearance, the QPO frequencies exhibit a monotonic increase from 73 mHz to 4 Hz (between points *a–d* in Fig. 1b). After reappearing, the QPOs show a decreasing trend (from 6.14 Hz to 3.26 Hz) over  $\sim 1.5$  days (between points *e–f*), which is typically seen during the declining phase of transient BH candidate outbursts. Subsequently, non-evolving sporadic QPOs are observed during the plateau epoch (E–F) of the outburst, a behavior commonly associated with the SIMS of transient BH-XRBs.

To investigate the shock-wave dynamics during the QPO evolution, we fitted the observed frequencies with the POS model, in which LFQPOs are considered to originate from oscillations of the shock. Important

phases of the POS model fitted QPO evolution is marked by points *a-f*. The model fit indicates that the shock moves inward toward the BH (from 1230 to 211  $r_s$ ) between points *a* and *d*, and recedes outward (from 151 to 226  $r_s$ ) between points *e* and *f*. A higher shock velocity is observed during the *a-b* and *e-f* phases. Additionally, the shock strength gradually weakens during the QPO increasing phase *a-d*, reaching a minimum compression ratio of  $R = 1$  at point *d*.

The observed QPO trends are broadly consistent with those commonly seen during the rising and declining harder spectral states (HS and HIMS) of transient BH candidates, where inward shock propagation (corresponding to increasing QPO frequency) and outward propagation (corresponding to decreasing QPO frequency) are typically observed. However, an outward shock motion associated with a monotonic decrease in the QPO frequency immediately following the end of the monotonic increase in the QPO evolution is uncommon. A similar short-duration QPO frequency decrease was recently reported in Swift J1727.8-1613 for  $\sim 1.2$  days within an overall increasing trend (D. Debnath et al. 2025). From a physical perspective, an outward-moving shock may occur when viscosity at the outer edge of the disk (i.e., at  $X_p$ ) decreases or is temporarily turned off, thereby reducing the supply of high-viscosity Keplerian matter, which constitutes the primary source of thermal soft X-ray photons. The roughly constant QPO frequency between *b* and *c*, after the initial rise, occurs due to the slow inward movement of the shock wave. This behavior is likely associated with a roughly constant or slowly increasing thermal Keplerian component, as seen in the SXR band. A similar feature was observed in the 1999 outburst of XTE J1859+226 (A. Nandi et al. 2018) and in the recent 2023–24 outburst of Swift J1727.8-1613 (D. Debnath et al. 2025).

To understand the nature of the source during the softest phase of the outburst, i.e., during the primary flare epoch, we performed broadband spectral analysis using one *Insight-HXMT* observation (on the peak day at point D; ObsID P081404800601) and one *NuSTAR* observation (ObsID 91202311002), marked as yellow and cyan shades in Fig. 1, respectively. We employed three model sets combining phenomenological and physical models. The phenomenological `diskbb+powerlaw` model provides a basic picture of the thermal and non-thermal components, but does not reveal the physical mechanisms behind their production. A prominent broad Fe emission line at  $\sim 6.5$  keV is observed in the *NuSTAR* spectrum (SPEC2). The higher disk temperature ( $T_{\text{in}} > 1.2$  keV) and photon index ( $\Gamma > 2.4$ ) indicate that the source was in the softer spectral states (HSS or SIMS) during the primary flare.

To investigate the properties of the ‘hot’ Compton cloud (corona), we replaced the `powerlaw` with the physical thermal Comptonization model (`thcomp`), defining model M2. However, this model along with a `gaussian`

component for the prominent Fe emission line, is found to adequately fit the nonthermal continuum, including the deviation in the higher-energy band ( $> 50$  keV) of SPEC2. The higher coronal temperature ( $kT_e$ ) and increased covering fraction in the second observation suggest an increase in both size and optical depth of the corona. The lower disk temperature ( $kT_{\text{in}}$ ) also indicates a comparatively harder spectral state. Furthermore, a decrease in thermal `diskbb` flux relative to the nonthermal `thcomp` flux suggests that the source became harder in the later *NuSTAR* observation, which explains the reappearance of the QPO during the *NuSTAR* observation period. Out of the total  $\sim 40$  ks *NuSTAR* observation period, the QPO at  $\sim 6.14$  Hz is significantly detected only after  $\sim 25$  ks.

Finally, spectral fitting with the relativistic `relxill` model provides a more detailed physical picture of the source. The `relxill+diskbb` model fits both spectra well, and no additional `powerlaw` component is required for SPEC2. The decrease in the thermal disk temperature ( $T_{\text{in}}$ ) and photon index ( $\Gamma$ ) in SPEC2 confirms that the source transitioned to a slightly harder state compared to SPEC1. Since SPEC1 corresponds to the softest phase, a higher cutoff energy ( $E_{\text{cut}}$ ) is observed. These results imply that the corona may have been smaller during SPEC1 of *Insight-HXMT*. The higher relativistic reflection fraction in SPEC1 is consistent with this scenario.

We also estimated intrinsic parameters, namely the spin ( $a_k$ ) and inclination angle ( $i$ ), from the spectral fits using model M3. For SPEC1, we obtained  $a_k = 0.998^{+p}_{-0.002}$  and  $i = (65.2^{+2.4}_{-2.1})^\circ$ . For SPEC2, we measured  $a_k = 0.998^{+p}_{-0.001}$  and  $i = (68.4^{+1.6}_{-1.8})^\circ$ . Combining these results, we predict the spin and inclination of the source to be  $a_k \sim 0.998$  and  $i \sim 63^\circ - 70^\circ$ . These measurements are consistent with earlier reports by A.M. El-Batal et al. (2016) and J. Casares et al. (2009).

Recent *IXPE* observations from 2026 Feb 7–9 detected a significant polarization degree of  $\sim 4\%$  at a polarization angle of  $\sim -1^\circ$  in the 2–8 keV energy band (S. Ravi et al. 2026). The spin and inclination derived from simultaneous spectral modeling of *IXPE* and *Insight-HXMT* data are consistent with the results presented here. A detailed spectro-polarimetric study has been performed and will be published elsewhere.

A brief summary of our findings in this *paper* is as follows:

- i) GS 1354-64 exhibited an unconventional outburst profile, characterized by two short-duration X-ray flares. The peak fluxes of the two flares were observed to be 1.4 and 0.8 Crab in the 2–20 keV band of *MAXI/GSC*.
- ii) The soft X-ray *MAXI/GSC* flux in 2–6 keV followed a trend similar to the total flux in 2–20 keV, while the hard X-ray flux in 6–20 keV remained

roughly constant. This indicates that thermal photons from the high-viscosity Keplerian disk were the primary component controlling the evolution of the spectral and temporal properties of the source.

- iii) The HID resembled the canonical rising phase of a transient BH candidate outburst. However, during the onset and decay phases of the primary flare, the hardness ratio (HR) retraced the same path, which is quite uncommon.
- iv) Strong signatures of LFQPOs were observed throughout the outburst (except for  $\sim 2$  days during the primary X-ray flare) where *Insight*-HXMT and *NuSTAR* data were available. Monotonic evolution of the QPO frequencies was observed up to the declining phase of the primary flare. Thereafter, non-evolving sporadic QPOs were observed for  $\sim 13$  days between the two flares.
- v) Fitting the QPO frequency evolution with the propagating oscillatory shock (POS) model allowed us to probe the nature of the shock, which is considered the origin of the LFQPOs according to the shock oscillation model. A stronger shock moved inward from  $1230 r_s$  to  $211 r_s$  and weakened during the monotonically increasing phase of the QPO frequency between 2026 Jan 1–27 (MJD 61053.61–61067.41). During the short flare decay phase (MJD 61070.33–61071.78), a weaker receding shock moved outward from  $151 r_s$  to  $226 r_s$ .
- vi) Detailed spectral analysis of two observations (one each from HXMT and NuSTAR) using both physical and phenomenological models indicates that the source was in the softer (HSS and/or SIMS) states during the primary flare.

vii) The source became slightly harder (within the softer spectral phase) in the later NuSTAR observation during the decay phase of the primary flare. This explains the reappearance of the LFQPO in the late epoch of the NuSTAR observation on 2026 Jan 30.

viii) Relativistic modeling with `relxill` estimates the spin and inclination angle as  $a_k \sim 0.998$  and  $i \sim 63^\circ\text{--}70^\circ$ , consistent with previous reports in the literature.

#### ACKNOWLEDGEMENTS

We are thankful to the anonymous referee and scientific Editor for kind suggestions to improve the quality of the paper. This work made use of on-demand data from *MAXI*, a Japanese Experiment Module on the International Space Station, and archival data from *Insight*-HXMT, a satellite mission of the China National Space Administration (CNSA) and the Chinese Academy of Sciences (CAS), as well as *NuSTAR*, a NASA observatory. The authors sincerely thank the MAXI team (RIKEN, JAXA) for providing on-demand data products and the HXMT team for providing the latest CALDB file (v2.08) prior to its official release. DD acknowledges the visiting research grant from National Tsing Hua University, Taiwan (NSTC 114-2811-M-007-084). HKC and SS acknowledge support from the National Science and Technology Council (NSTC) of Taiwan under grant NSTC 114-2112-M-007-042. AN thanks GH, SAG; DD; PDMSA; and the Director, URSC, for encouragement and continuous support in carrying out this research. We also thank the instrument teams for processing the data and providing the necessary software tools for the analysis.

#### REFERENCES

- Adegoke, O. K., Garcia, Javier A., Tomsick, J. A., et al., 2026, ATel, 17612, 1
- Bambi C. et al., 2021, Space Sci. Rev., 217, 65
- Bhowmick, R., Debnath, D., Chatterjee, K., et al., 2021, ApJ, 910, 138
- Brenneman L. W., Reynolds C. S., 2006, ApJ, 652, 1028
- Belloni, T., Homan, J., Casella, P., et al., 2005, A&A, 440, 207
- Casares J., Zurita C., Shahbaz T., Charles P. A., Fender R. P., 2004, ApJ, 613, L133
- Casares J. et al., 2009, ApJS, 181, 238
- Casella, P., Belloni, T., & Stella, L., 2005, ApJ, 629, 403
- Chakrabarti, S. K. & Titarchuk, L. G., 1995, ApJ, 455, 623
- Chakrabarti, S. K., 1996a, Physics Reports, 266, 229
- Chakrabarti, S. K., 1996b, ApJ, 464, 664
- Chakrabarti, S.K., Debnath, D., Nandi, A., Pal, P. S., 2008, A&A 489, L41
- Chakrabarti S. K., Mondal, S. Debnath, D., 2015, MNRAS, 452, 3451
- Chakrabarti, S. K., Debnath, D., Nagarkoti, S., 2019, AdSpR, 63, 3749
- Chatterjee, K., Debnath D., Bhowmick, R., et al., 2022, MNRAS, 510, 1128
- Choudhury, S. D., Bhuvana, G. R., Das, S., 2025, MNRAS, 541, 2934
- Debnath, D., Chakrabarti, S. K., i& Nandi, A., 2010, A&A, 520, 98
- Debnath, D., Chakrabarti, S.K., & Nandi, A., 2013, AdSpR, 52, 2143
- Debnath, D., Mondal, S., & Chakrabarti, S.K., 2015, MNRAS, 447, 1984

- Debnath, D., Jana, A., Chakrabarti, S. K., Chatterjee, D., & Mondal, S., 2017, *ApJ*, 850, 52
- Debnath, D., in *Exploring the Universe: From Near Space to Extra-galactic Mukhopadhyay, B & Sasmal, S. (Eds.)*, 2018, *ASSP*, 53, 229, Springer (Heidelberg)
- Debnath, D., Srimani, S., & Chang, H.K., 2025, *ApJ*, 989, 165
- D. Debnath, S. Srimani, A. Nandi, H. K. Chang, 2026 (in preparation)
- Done, C., Gierliński, M., Kubota, A., 2007, *A&ARv* 15, 1
- Ebisawa, K., Titarchuk, L., Chakrabarti, S. K., 1996, *PASJ*, 48, 59
- El-Batal, A. M., Miller, J. M., Reynolds, M. T., et al., 2016, *ApJL*, 826, L12
- Fabian, A.C., Rees, M.J., Stella, L., White, N.E., 1989, *MNRAS* 238, 729
- Fender, R. P., Belloni, T. M., Gallo, E., 2004, *MNRAS*, 355, 1105
- Francey R. J., 1971, *Nat. Phys. Sci.*, 229, 228
- Galeev, A. A., Rosner, R., & Vaiana, G. S. 1979, *ApJ*, 229, 318
- García J., Kallman T. R., 2010, *ApJ*, 718, 695
- Haardt, F., & Maraschi, L. 1993, *ApJ*, 413, 507
- F. A. Harrison, W. W. Craig, F. E. Christensen, et al. 2013, *ApJ*, 770, 103
- Homan, J. & Belloni, T., 2005, *Ap&SS*, 300, 107
- Iyer, N., Nandi, A., Mandal, S., 2015, *ApJ*, 807, 108
- Jana, A., Debnath, D., Chakrabarti, S. K., et al. 2016, *ApJ*, 819, 107
- Kitamoto S., Tsunemi H., Pedersen H., et al., 1990, *ApJ*, 361, 590
- Kalberla P. M. W., Burton W. B., Hartmann D., et al., 2005, *A&A*, 440, 775
- Lightman, A.P., White, T.R., 1988, *ApJ* 335, 57
- Liu, H., Kong, L., Adegoke, O. K., et al., 2026 (arXiv:2026arXiv260306883L)
- Makishima, K. Maejima, Y., Mitsuda, K., et al. 1986, *ApJ*, 308, 635
- Makishima, K. 1986, *Lecture Notes in Physics*, 266, 249
- Makino F., 1987, *IAU Circ.*, 4342, 1
- Markert T. H. et al., 1979, *ApJS*, 39, 573
- Mitsuda, K., Inoue, H., Koyama, K. et al., 1984, *PASJ*, 36, 741
- Molteni D., Sponholz H., Chakrabarti S. K., 1996, *ApJ*, 457, 805
- Nandi, A., Debnath, D., & Mandal, S., et al., 2012, *A&A*, 542, 56
- Nandi, A., Mandal, S., Sreehari, H., et al., 2018, *Ap&SS*.363, 90
- Negoro, H., Fujiwara, K., Nakajima, M., et al., 2025, *ATel*, 17563, 1
- Negoro, H., Nakajima, M., Takagi, K., et al., 2026, *ATel*, 17618, 1
- Radhika, D, Nandi, A., Agrawal, A. K., Seetha S., 2016, *MNRAS*, 460, 4403
- Remillard, R. A., & McClintock, J. E., 2006, *ARA&A*, 44, 49
- Ravi, S., Marra, L., Steiner, J. F., et al., 2026 (arXiv:2026arXiv260303463R)
- Reynolds, C. S., 2014, *Space Science Reviews*, 183, 277
- Ryu, D., Chakrabarti, S. K., Molteni, D., 1997, *ApJ*, 474, 378
- Shakura, N. I., & Sunyaev, R. A. 1973, *A&A*, 24, 337
- Sreehari, H., Iyer, N., Radhika, D., et al., 2019, *AdSpR*, 63, 1374
- Sreehari, H. & Nandi, A, 2021, *MNRAS*, 502, 1334
- Stella L., Vietri M., 1999, *NuPhS*, 69, 135
- Stiele, H., Belloni, T. M., Kalemci, E., et al., 2013, *MNRAS*, 429, 2655
- Sunyaev R. A., Titarchuk L. G., 1980, *ApJ*, 86, 121
- Sunyaev R. A., Titarchuk L. G., 1985, *A&A*, 143, 374
- Swinbanks D., 1987, *Nature*, 326, 322
- Tanaka, Y. & Lewin, W. H. G., 1995, *X-ray Binaries*, Publication by Nasa, p. 126-174
- Tanaka, Y., & Shibazaki, N. 1996, *ARA&A*, 34, 607
- Tetarenko, B. E., Sivakoff, G. R., Heinke, C. O., & Gladstone, J. C. 2016, *ApJS*, 222, 15
- Titarchuk L., Lapidus I., Muslimov A., 1998, *ApJ*, 499, 315
- Titarchuk, L., & Seifina, E., 2009, *ApJ*, 706, 1463
- Varnière P., Tagger M., 2002, *A&A*, 394, 329
- Veledina, A., Vurm, I., Poutanen, J., 2011, *MNRAS* 414, 3330
- Vignarca, F.; Migliari, S.; Belloni, T., 2003, *A&A*, 397, 729
- Wardziński, G., Zdziarski, A.A., 2000, *MNRAS* 314, 183
- Zdziarski, A. A., Lubinski, P., Gilfanov, M., et al. 2003, *MNRAS*, 342, 355
- Zhang, S., Lu, F.J., Zhang, S.N., et al., 2014. In: *Space Telescopes and Instrumentation 2014: Ultraviolet to Gamma Ray*. In: *Proc. SPIE*, vol. 9144, 914421
- Zhang, S.-N., Li, T., Lu, F., et al. 2020, *SCPMA*, 63, 249502